

7 ABSTRACT: Diabatic Rossby Vortices (DRVs) are a special class of heavily precipitating extra-
8 tropical cyclone in which latent heating effects play a key role. As such their dynamics defies the
9 classic mechanism of midlatitude storm formation and poses challenges to modelling and theoret-
10 ical understanding. Here we build on recent theoretical advances on the growth of DRV modes in
11 small-amplitude moist instability calculations by exploring the structure of finite-amplitude DRV
12 storms in a hierarchy of models of moist macroturbulence. Simulations of moist quasigeostrophic
13 turbulence show a transition to a DRV dominated flow (DRV world) when the latent heating is
14 strong. The potential vorticity (PV) structure of the DRVs is similar to the PV structure from
15 small-amplitude DRV modal theory. Simulations of the moist primitive equations also transition
16 to DRV world when both the latent heating is strong and the Rossby number is sufficiently low. At
17 high Rossby numbers, however, the PV structure of storms with strong latent heating is bottom-
18 intensified compared to DRV modal theory due to higher order effects beyond quasigeostrophy,
19 and the macroturbulent flow has both DRV-like storms and frontal structures. A 1-D model of the
20 vertical structure of PV is solved for different Rossby numbers and stratification profiles to reconcile
21 the PV structures of DRVs in the simulations, small-amplitude modal theory, and observations.

22 SIGNIFICANCE STATEMENT: Diabatic Rossby Vortices (DRVs) are a special class of heavily
23 precipitating extratropical cyclones which grow from the effects of latent heating and as such go
24 beyond the classic growth mechanism of midlatitude storm formation. DRVs have been implicated
25 in extreme and poorly predicted forms of cyclogenesis and pose challenges to both modeling and
26 theoretical understanding. Here, we extend our previous study on the structure and emergence of
27 DRVs in small-amplitude instability calculations by exploring the structure of DRV storms and the
28 conditions for the emergence of DRV dominated atmospheres ('DRV world') in a range of different
29 finite-amplitude simulations.

30 1. Introduction

31 Past research has identified a special class of midlatitude storm, dubbed the Diabatic Rossby
32 Vortex (DRV)¹, which derives its energy from the release of latent heat associated with condensation
33 of water vapor, and as such differs fundamentally from the traditional understanding of midlatitude
34 storm formation (Wernli et al. 2002; Moore and Montgomery 2004, 2005; Moore et al. 2008).
35 DRVs have been implicated in extreme and poorly predicted forms of cyclogenesis along the east
36 coast of the US and the west coast of Europe with significant damage to property and human life
37 (Wernli et al. 2002; Boettcher and Wernli 2013; Moore et al. 2008). DRVs have been identified in
38 all oceans basins and seasons, and occur at a rate of roughly 10 systems per month in the Northern
39 Hemisphere and 4 systems per month in the Southern Hemisphere (Boettcher and Wernli 2013,
40 2015).

41 More recently, moist baroclinic instability calculations with an idealized GCM over a wide range
42 of climates have shown that DRVs become the dominant mode of moist baroclinic instability in
43 sufficiently warm climates, pointing to the increased role DRVs might play in the development
44 of fast growing disturbances in a warming climate (O’Gorman et al. 2018). While we have a
45 good theoretical understanding of classic cyclogenesis, both in terms of simple conceptual models
46 of baroclinic instability (Eady 1949; Charney 1947; Phillips 1954; Emanuel et al. 1987; Fantini
47 1995; Zurita-Gotor 2005,) and potential vorticity (PV) dynamics of finite-amplitude storms (Davis
48 and Emanuel 1991), we have less understanding of the formation and propagation of DRVs, the
49 controls on their growth rates and length scales, and their response under climate change. Given

¹DRVs are also referred to as Diabatic Rossby Waves.

50 the importance of diabatic effects in cyclogenesis in the current climate and more so in a warming
51 climate, developing an equivalent theoretical understanding for DRVs is critical.

52 In a recent paper, we isolated the DRV growth mechanism within a conceptually simple and
53 analytically tractable model and used it to derive theoretical results for the growth rate and length
54 scale of such disturbances (Kohl and O’Gorman 2022). The model was a moist two-layer quasi-
55 geostrophic (QG) system in which the effects of latent heating were represented through a reduction
56 of the static stability in updrafts in the spirit of simple moist baroclinic theories (Emanuel et al.
57 1987). The boundaries were tilted at a variable slope relative to the mean isentrope, thereby
58 allowing us to control the strength of meridional PV advection relative to diabatic generation from
59 latent heating. In particular this allowed us to study a pure latent-heating driven disturbance with
60 no meridional PV advection. We showed that DRVs emerge as the fastest growing modes of moist
61 baroclinic instability when the meridional PV gradients is weak and the moist static stability is
62 also sufficiently weak (i.e., the latent heating is sufficiently strong). Furthermore, we developed
63 a simple PV argument to explain the transition from wave to vortex modes observed in idealized
64 GCM simulations of warm climates (O’Gorman et al. 2018). Finally, analytical solutions were
65 derived for a DRV mode in an unbounded domain, and a threshold of $r = 0.38$ was found above
66 which DRV solutions cease to exist.

67 While the two-layer QG results in Kohl and O’Gorman (2022) makes progress on the growth
68 mechanism and PV structure of DRV modes, they are based around an assumption of small
69 amplitude disturbances, and the implications for finite amplitude disturbances require further in-
70 vestigation. Comparing the structure of DRV modes to DRV storms in current and future climates,
71 for instance, we showed that finite amplitude effects (e.g., vertical PV advection, ageostrophic
72 advection) must be taken into account to relate the structure of PV anomaly and diabatic gener-
73 ation in certain observed storms (Kohl and O’Gorman 2022). Furthermore, the small-amplitude
74 instability results from the idealized GCM show that the fastest growing mode transitions to a DRV
75 rather than a wave in warm climates, but the corresponding macroturbulent state in the idealized
76 GCM remains wavy and is not dominated by DRVs (O’Gorman et al. 2018), even if DRVs can be
77 identified (Kohl and O’Gorman 2022). It remains unclear if a macroturbulent flow at statistical
78 equilibrium with strong latent heating can transition to a completely DRV dominated flow, which
79 we will refer to as a ‘DRV world’ from here on.

80 The goal of this paper is to go beyond small-amplitude DRV modes and study the dynamics
81 of finite amplitude DRVs and the potential for a transition to DRV world in a hierarchy of dif-
82 ferent models of moist macroturbulence, including simulations of moist macroturbulence using
83 the quasigeostrophic equations, simulations of moist macroturbulence using the primitive equa-
84 tions, and a simple 1D model for the vertical structure of PV in small-amplitude DRV modes vs.
85 finite-amplitude storms. The spirit of the simulations is to keep the representation of moist physics
86 as simple as possible by sticking to the reduced stability parameterization of latent heating from
87 modal theory (Emanuel et al. 1987, Fantini 1995, Kohl and O’Gorman 2022), while gradually
88 introducing higher order terms in the dynamics beyond that of small-amplitude modal theory. The
89 work is deliberately phenomenological, studying large parameter ranges in a range of different
90 models so as to explore the conditions leading to a clear transition to DRV world and to explore
91 the differences between the behavior of small-amplitude modes and finite amplitude storms.

92 In section 2, we begin by analyzing simulations of moist quasigeostrophic (QG) turbulence as
93 a natural extension of the 2-layer moist quasigeostrophic theory of DRV modes presented in Kohl
94 and O’Gorman (2022). The QG simulations parallel the work of Lapeyre and Held (2004), but
95 with a reduced stability parameterization for latent heating (Emanuel et al. 1987) which greatly
96 reduces the number of parameters involved and allows for better comparison with the work of
97 O’Gorman et al. (2018) and Kohl and O’Gorman (2022). We show that the flow transitions from
98 a state of wavy jets interspersed with vortices to a vortex dominated flow (‘DRV world’) as the
99 latent heating is increased. By analyzing the PV structure and PV budget of the storms in the
100 strong latent heating regime of the QG simulations, we confirm that the flow has transitioned to
101 DRV world. In section 3, we study moist primitive equation simulations in low, intermediate
102 and high Rossby number regimes to explore the effects of higher-order effects beyond QG on the
103 structure of diabatically driven storms and the overall character of the macroturbulent circulation.
104 The simulations are an attempt to bridge the gap between theoretical studies of DRVs based around
105 the moist-quasigeostrophic equations versus GCM simulations and observations. In particular,
106 strong latent heating is found to lead to a DRV world at low Rossby number but not at high Rossby
107 number. In section 4, we distill higher-order effects into a toy model of the vertical structure of
108 PV in DRVs that is solved to reproduce much of the variety of the PV structure of DRV storms

109 from the simulations in the previous two sections of the paper and also from reanalysis (Kohl and
 110 O’Gorman 2022). In section 5, we summarize our results and discuss future work.

111 2. DRVs in Simulations of Moist Quasigeostrophic Turbulence

112 a. Model Formulation and Governing Equations

113 A natural extension of the two-layer moist quasigeostrophic theory of DRV modes presented
 114 in Kohl and O’Gorman (2022) is to run simulations of moist quasigeostrophic turbulence. The
 115 two-layer moist QG equations with equal layer height, β -plane approximation and low level drag
 116 take the nondimensional form

$$\partial_t \nabla^2 \phi + J(\phi, \nabla^2 \phi) + J(\tau, \nabla^2 \tau) + \beta \phi_x = -\frac{R}{2} \nabla^2 (\phi - \tau), \quad (1)$$

$$\partial_t \nabla^2 \tau + J(\phi, \nabla^2 \tau) + J(\tau, \nabla^2 \phi) + \beta \tau_x + w = \frac{R}{2} \nabla^2 (\phi - \tau), \quad (2)$$

$$\partial_t \tau + J(\phi, \tau) + r(w)w = \overline{r(w)w}, \quad (3)$$

117 with barotropic and baroclinic stream function $\phi = \frac{\psi_1 + \psi_2}{2}$ and $\tau = \frac{\psi_1 - \psi_2}{2}$ where ψ_1 refers to the
 118 streamfunction in the upper layer and ψ_2 to the streamfunction in the lower layer, and with Jacobian
 119 $J(A, B) = A_x B_y - A_y B_x$ and domain mean average $\overline{(\dots)}$. Here, $R = R_{dim} L_D / U$ where R_{dim} is the
 120 dimensional drag coefficient, and $\beta = \beta_{dim} L_D^2 / U$ where β_{dim} is the dimensional β parameter. The
 121 equations have been nondimensionalized assuming an advective time scale, with the deformation
 122 radius $L_D = NH / (\sqrt{2}f)$ as the length scale, where H is the layer height, and U as the velocity scale
 123 which is equivalent to the zonal velocity in the basic static described below (U in the top layer, and
 124 $-U$ in the bottom layer).² The effects of latent heating on the dynamics are encapsulated in the
 125 spirit of simple moist theories (Emanuel et al. 1987; Fantini 1995) by the nonlinear factor

$$r(w) = \begin{cases} r, & w \geq 0 \\ 1, & w < 0 \end{cases} \quad (4)$$

²Discretizing the continuous thermodynamic equation leads to a deformation radius involving N , rather than a reduced gravity, at the mid-tropospheric level.

126 which reduces the static stability by a factor r in regions of ascent. Physically, the nonlinear factor
 127 $r(w)$ captures that as moist air ascends, it releases latent heat through condensation, resulting in
 128 a locally reduced static stability. Conversely, descending air, having undergone precipitation and
 129 become subsaturated, experiences the full static stability. Moist thermodynamics thus introduces
 130 an additional nonlinearity into the equations which can lead to interesting dynamics. The term
 131 $\overline{r(w)w}$ in Eq. 3 acts as a spatially uniform radiative cooling to ensure that the domain-mean
 132 temperature remains constant even though there is latent heating. Eqs. (1-3) are obtained from
 133 Eqs. A6-A8 in Kohl and O’Gorman (2022) after setting the boundaries at top and bottom to be
 134 horizontal $h_1 = h_2 = 0$, and including the β effect and low level drag.

135 The system is allowed to go moist baroclinically unstable about a mean temperature gradient in
 136 thermal wind balance, which corresponds to $\tau_0 = -y$, $\phi_0 = 0$ and $w_0 = 0$. We set $\tau = \tau_0 + \tau'$, $\phi = \phi'$,
 137 and $w = w'$. Eqs. (1-3) then take the form

$$\partial_t \nabla^2 \phi + J(\phi, \nabla^2 \phi) + J(\tau, \nabla^2 \tau) + \beta \phi_x = -\nabla^2 \tau_x - \frac{R}{2} \nabla^2 (\phi - \tau) - \mu \nabla^4 (\nabla^2 \phi), \quad (5)$$

$$\partial_t \nabla^2 \tau + J(\phi, \nabla^2 \tau) + J(\tau, \nabla^2 \phi) + w + \beta \tau_x = -\nabla^2 \phi_x + \frac{R}{2} \nabla^2 (\phi - \tau) - \mu \nabla^4 (\nabla^2 \tau), \quad (6)$$

$$\partial_t \tau + J(\phi, \tau) + r(w)w = \phi_x - \mu \nabla^4 \tau - \alpha \tau + \overline{r(w)w} \quad (7)$$

138 where we have dropped all the primes for notational simplicity, and ϕ , τ and w represent pertur-
 139 bations about the basic state that have spatially homogeneous statistics. The horizontal means of
 140 the stream functions ϕ and τ , and the mean of w are all enforced to be zero. Setting the mean
 141 of τ to zero is equivalent to including the spatially uniform radiative cooling term $\overline{r(w)w}$. Eqs.
 142 (5-7) also include a small-scale dissipation parametrized by a fourth-order hyper-diffusion with
 143 coefficient μ ; and a large-scale radiative damping parameterized by a linear Newtonian relaxation
 144 with coefficient α . The large-scale radiative damping was found to be necessary for simulations
 145 with roughly $r < 0.4$ and thus large energy input from latent heating because the linear drag term
 146 was not enough to remove the energy at large scales and allow the simulations to reach a statistical
 147 steady state (see section 2d for further details), The inability of the static stability to adjust in QG
 148 and the imposition of a fixed meridional temperature gradient make for a particularly simple and
 149 homogeneous model setup for analysis, but they also tend to limit the ability of the QG model to
 150 equilibrate.

151 Our system of moist QG equations differs from the moist QG equations of Lapeyre and Held
152 (2004) primarily by always assuming upward motion to be saturated. Thus, no prognostic moisture
153 equation is needed, and the effects of latent heating are captured in terms of a single parameter r .
154 So far the r parametrization has been used in studies of moist baroclinic instability as an initial
155 value problem (Emanuel et al. 1987, Montgomery and Farrell 1991, Montgomery and Farrell 1992,
156 Fantini 1995, Moore and Montgomery 2004, Kohl and O’Gorman 2022) with the exception of
157 O’Gorman et al. (2018) which considered both small-amplitude instability and a macroturbulent
158 steady state. To our knowledge, this is the first time that the r -parametrization has been applied
159 to macroturbulent simulations in a two-layer model. We choose this system here for its simplicity
160 and ease of comparison to moist baroclinic theories, but acknowledge that having a prognostic
161 moisture equation, like in Lapeyre and Held (2004), allows for conservation properties that are
162 more desirable when developing closure theories for PV fluxes (which is not our focus here).

163 *b. Numerical Simulations: Dry vs. Moist Regimes*

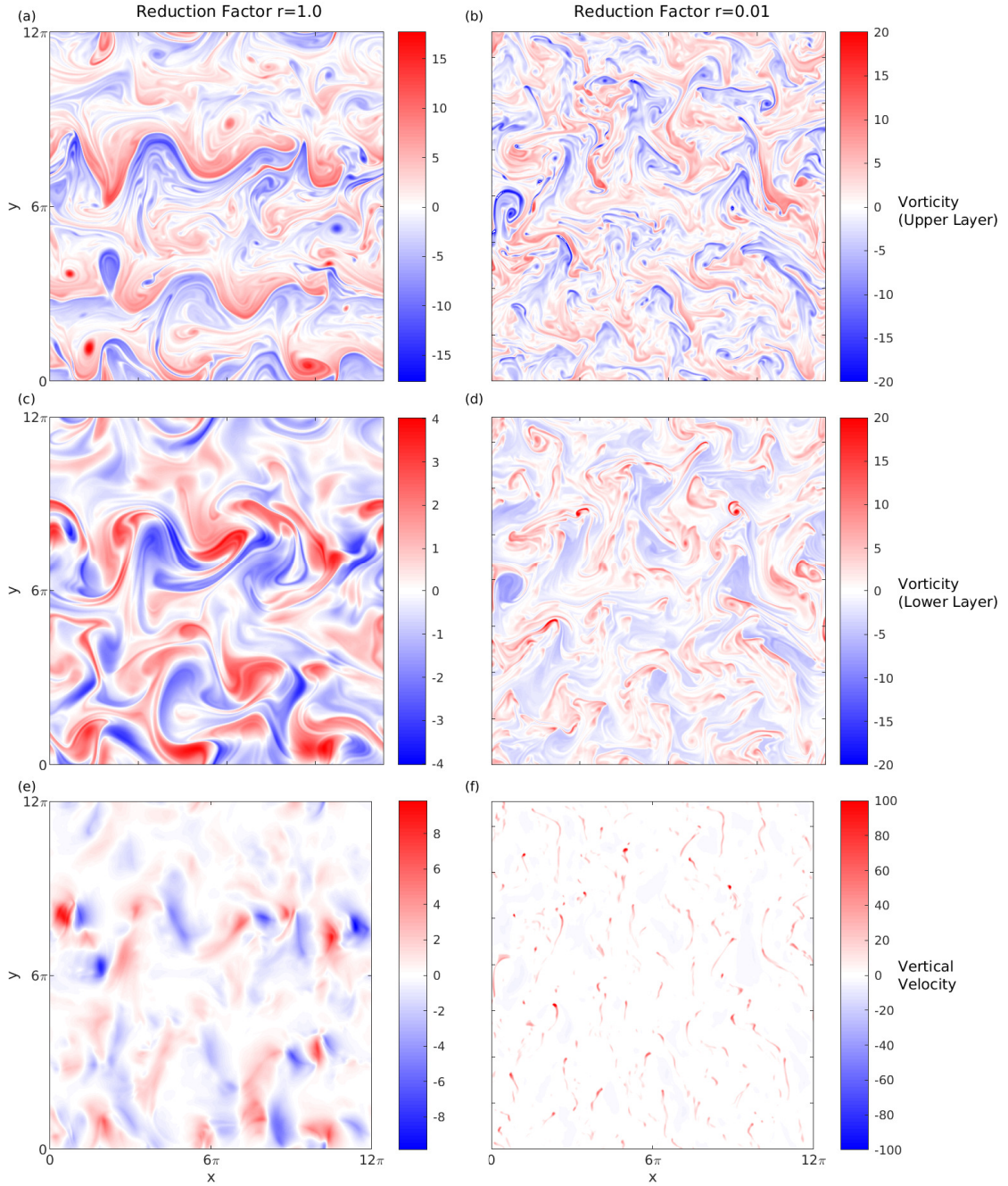
164 We solve the moist two-layer QG Eqs. (5-7) on a doubly-periodic domain of size $L = 12\pi$ with
165 512×512 grid points using Dedalus, a flexible framework for numerical simulations with spectral
166 methods (Burns et al. 2020). We show results for simulations with $r = 1$ (a dry simulation) and
167 $r = 0.01$ (a moist simulation with strong latent heating). We fix $\beta = 0.78$ equal to the value of
168 Lapeyre and Held (2004).³ This corresponds to a moderate dry supercriticality of $\chi = \beta^{-1} = 1.28$,
169 where $\chi > 1$ is required for the inviscid dry model to go unstable. We set $R = 0.11$ and $\mu = 10^{-5}$
170 for both values of r . We set $\alpha = 0$ for $r = 1$ and $\alpha = 1.7$ for $r = 0.01$. The simulations are started
171 using random initial conditions for the stream functions ϕ and τ , where we have filtered out all
172 wavenumbers with $k = \sqrt{k_x^2 + k_y^2} > 3$ to avoid having to integrate a lot of small scale noise in the
173 initial phase of the simulation. The simulations are run from $t = 0$ until $t = 120$ at $r = 0.01$ and
174 $t = 150$ at $r = 1$ and outputted in snapshots at time intervals of 0.25. After an initial phase of modal
175 instability, the simulations settle into a macroturbulent state (roughly at $t = 40$ for $r = 0.01$ and
176 $t = 60$ at $r = 1$). This happens more quickly at $r = 0.01$ because the growth rate of the modes is
177 increased by latent heating.

³Please note that compared to Lapeyre and Held (2004), our deformation radius is defined as $L_D = NH/(\sqrt{2}f)$ instead of $L_D = NH/f$ but the magnitude of our mean flow is U instead of their $U/2$ so that the definition of $\beta = \beta_{dim} L_D^2/U$ is equivalent.

183 We begin by comparing the structure of the flow field in the two simulations. The relative
184 vorticity in the upper and lower layer, alongside the vertical velocity are shown in Fig. 1. Looking
185 at the dry simulation (Fig. 1a,c,e), we see that the flow settles into the well known state of β -plane
186 turbulence: wavy jets interspersed with vortices. The relative vorticity is weaker in the lower than
187 upper layer because of the low level drag. The vertical velocity field has large-scale ascending and
188 descending regions of similar area and magnitude that are mostly confined to the latitude bands of
189 the jets. We have provided an animation in Supplemental Video S1.

190 In contrast to the dry simulation, we see that the flow in the moist simulation at $r = 0.01$ (Fig.
191 1 b, d, f) has transitioned to a DRV world that is dominated by small scale vortices, despite
192 the presence of β . In fact when the simulation was run with β changed down to $\beta = 0$ or up
193 to $\beta = 1.5$, there was no noticeable effect on the overall flow field (not shown). As explored
194 in the next section, tendencies in the PV budget at this low $r = 0.01$ are dominated by diabatic
195 generation, nonlinear advection and drag, so that making changes to β like this are unimportant.
196 Indeed, the unimportance of advection across the mean meridional PV gradient in the simulation
197 is consistent with a vortex dominated rather than wavy flow. The vortices propagate northwards in
198 our simulations through nonlinear advection and the trails of this propagation can be seen in the
199 form of tendrilly north-south structures that are easiest to see in the vertical velocity field. This
200 is particularly evident by looking at a video of the evolution of the flow over time (Supplemental
201 Video S2).

202 The vertical velocity field in the moist QG simulation has narrow regions of strongly ascending
203 motion compared to wide regions of weakly descending motion (Fig. 1 f), corresponding to a
204 remarkably high vertical-velocity asymmetry parameter (O’Gorman 2011) of $\lambda = 0.94$. By contrast
205 the asymmetry parameter is much lower at $\lambda = 0.73$ for idealized GCM simulations at the same
206 $r = 0.01$ (O’Gorman et al. 2018). Kohl and O’Gorman (2024) introduced a simple toy model for λ
207 in macroturbulent flow based on the moist QG omega equation which was able to roughly predict
208 λ in the idealized GCM simulations and in reanalysis data. The key assumption of the toy model
209 is that the dynamical forcing on the right-hand side of the moist omega equation is unskewed for
210 macroturbulent flow, and this is found to also be the case in the QG simulations shown here. The
211 toy model for λ correctly predicts that the QG simulations have a higher λ than the idealized GCM



178 FIG. 1. Snapshots of relative vorticity in the upper layer (a,b) and lower layer (c,d), and vertical velocity (e,f)
 179 in the moist two-layer QG simulations at statistical equilibrium for $r = 1.0$ (a,c,e) and $r = 0.01$ (b,d,f). The flow
 180 transitions from a wavy jet state interspersed with vortices at $r = 1.0$ to a vortex dominated flow at $r = 0.01$. The
 181 vortices migrate poleward over time leaving a trail that can be seen in the vertical velocity snapshot in (f) and
 182 also more clearly over time in Supplementary Video S2.

212 because the overall length scale of the flow becomes smaller when the vortex regime emerges,⁴
 213 illustrating that high λ is in principle possible in macroturbulent flow even if it is not seen so far in
 214 reanalysis or in GCM simulations.

215 A similar transition to a vortex dominated state in the strong latent heating regime has first been
 216 observed by Lapeyre and Held (2004) in a moist-two layer QG system using prognostic moisture.
 217 However, the authors found that strong vortices had the same sign of vorticity in both layers (even if
 218 the upper layer vorticity was weaker), and the vorticity field had a much stronger tendency towards
 219 cyclones in the lower layer than towards anticyclones in the top layer. As we will see in the next
 220 section, the vortices in our simulation have a baroclinic structure consisting of dipoles of positive
 221 PV anomalies in the lower layer and negative PV anomalies in the upper layer and the tendency
 222 towards cyclones in the lower layer is roughly as strong as the tendency towards anticyclones in
 223 the top layer. Further work comparing simulations with the r parameterization of latent heating vs.
 224 prognostic moisture equations would be helpful to better understand these differences.

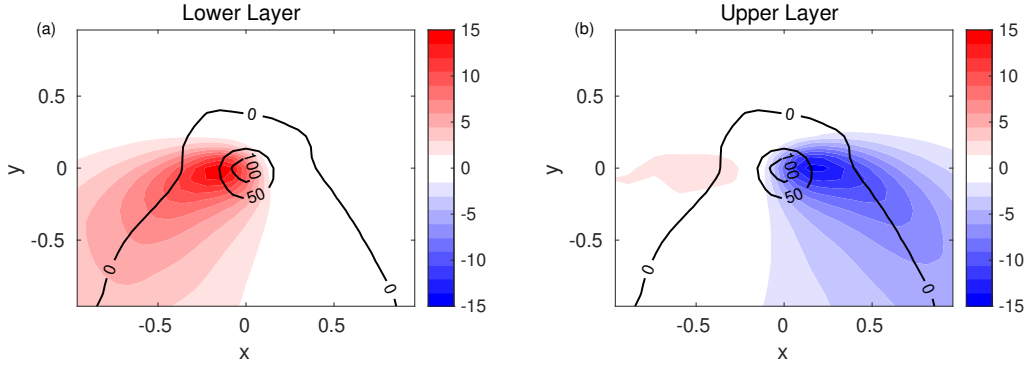
225 *c. Storm Composites of PV and Dynamical Balances in DRV World*

226 Fig. 2 shows the storm composite of PV anomaly and vertical velocity field in the upper and
 227 lower layer of the moist QG runs at $r = 0.01$. Composites were created by averaging over the 10
 228 strongest vertical velocity maxima at each simulation output time between $t = 40 - 120$ when the
 229 simulation had reached a macroturbulent state. The PV takes on the typical dipole structure of
 230 DRV modes with a positive PV anomaly in the lower layer and a negative PV anomaly in the top
 231 layer (e.g., Kohl and O’Gorman 2022). The PV anomalies are displaced horizontally such that the
 232 updraft occurs east of the low level positive PV anomaly and west of the upper level negative PV
 233 anomaly. The ‘trails’ of PV can be seen to go southward because the storms are moving northward.

239 Further insights into the dynamical balances maintaining the storms can be obtained by studying
 240 the tendencies in the PV budget. In the lower layer, the PV budget is given by

$$\partial_t q_2 = q_{2x} - v_2 \bar{q}_{2y} - J(\psi_2, q_2) + (1 - r(w))w - R\nabla^2 \psi_2, \quad (8)$$

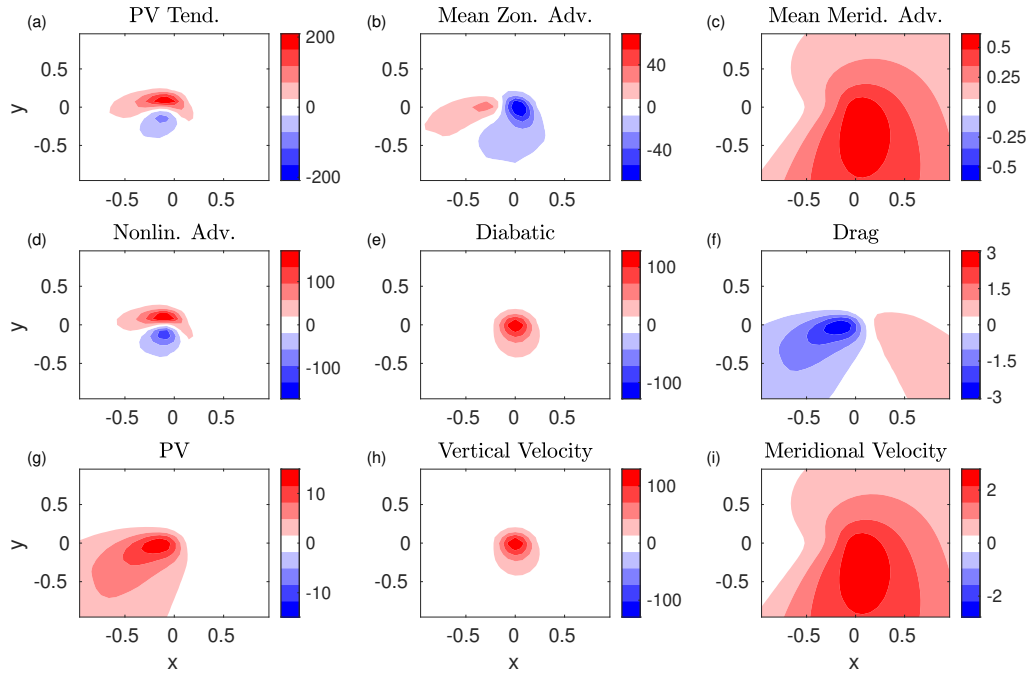
⁴The effective wavenumber of the w -spectrum, as defined in Kohl and O’Gorman (2024), is much larger in the QG simulations compared to the idealized GCM simulations ($k = 6.1$ vs. $k = 1.7$). Given these k values and $r = 0.01$, the toy model of Kohl and O’Gorman 2024 predicts a higher value of $\lambda = 0.84$ for the QG simulations compared to a prediction of $\lambda = 0.75$ for the GCM simulation. The underestimate of λ in the QG simulations by the toy model is likely a result of the fact the toy model is 1D whereas the vertical velocity field in the QG simulations has a more 2D structure (vortices) compared to the 1D structure (fronts) in the idealized GCM. A 2D version of the toy model predicts a value of the asymmetry of $\lambda = 0.92$ for the QG simulations which is in good agreement with the simulated value of $\lambda = 0.94$.



234 FIG. 2. Storm composite of the PV anomaly (shading) in (a) the lower layer, and (b) the upper layer of the
 235 moist QG turbulence simulations at $r = 0.01$. The vertical velocity is also shown (black contour); note negative
 236 velocities are too weak to be shown at the chosen contour interval of 50. Composites were created by averaging
 237 over the 10 strongest vertical velocity maxima at each simulation output between $t = 40 - 120$ when the simulation
 238 had reached a macroturbulent state.

248 where $q_2 = \nabla^2 \psi_2 + (\psi_1 - \psi_2)/2$ is the PV anomaly in the lower layer, $\partial_t q_2$ is the time tendency
 249 of the PV in the lower layer, q_{2x} is PV advection by the mean zonal wind, $-v_2 \bar{q}_{2y}$ is advection
 250 of the mean PV gradient by the meridional wind (\bar{q}_{2y} includes contributions from both the mean
 251 temperature gradient and β), $-J(\psi_2, q_2)$ is the nonlinear advection, $(1 - r(w))w$ is the diabatic PV
 252 tendency, and $-R\nabla^2 \psi_2$ is the drag term. We have ignored the radiative damping and hyperdiffusion
 253 terms which were found to be small. The composite of the PV tendencies in the lower layer are
 254 shown in Fig. 3 centered on the vertical velocity maxima. As can be seen from Fig. 3a, the
 255 net effect of all tendencies is to give poleward propagation and amplification of the PV anomaly.
 256 The PV tendencies are dominated by mean zonal PV advection, nonlinear advection and diabatic
 257 heating. Both the drag term, and the meridional advection of mean meridional PV gradients play a
 258 negligible role. This confirms the strong diabatic character of the storms in this regime with small
 259 r and thus strong latent heating.

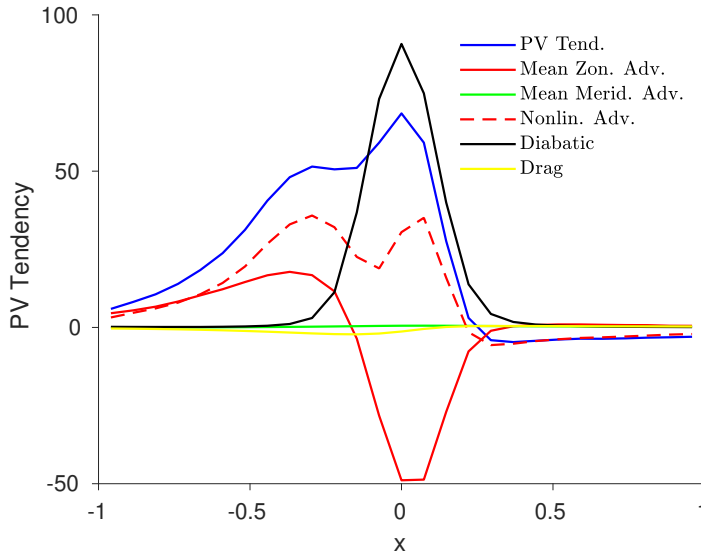
264 Fig. 4 shows a cross-section through the PV tendencies of Fig. 3 averaged between $-0.2 <$
 265 $y < 0.2$. From left to right, we observe that in the descending part of the solution to the west
 266 ($-1 < x < -0.4$), where the diabatic generation is zero, the PV tendency is given by the sum
 267 of mean zonal and nonlinear advection (with nonlinear advection the slightly more dominant
 268 contribution). In the ascending part of the solution ($-0.4 < x < 0.4$), the PV tendency is the result
 269 of a three way balance between diabatic generation, zonal advection and nonlinear advection. Here



241 FIG. 3. Composite of the PV tendencies in the lower layer for the storms in the two-layer moist QG turbulent
 242 simulation at $r = 0.01$ showing (a) PV tendency q_{2t} , (b) mean zonal advection q_{2x} , (c) mean meridional advection
 243 $-v_2 \bar{q}_{2y}$, (d) nonlinear advection $-J(\psi_2, q_2)$, (e) diabatic generation $(1 - r(w))w$, (f) drag $-R\nabla^2 \psi_2$. Also shown
 244 to help interpretation are (g) the lower-layer PV q_2 , (h) midlevel vertical velocity w , and (i) lower-layer meridional
 245 velocity v_2 . Note also that the mean zonal wind in the lower layer is westward. Composites were created by
 246 averaging over the 10 strongest vertical velocity maxima at each simulation output between $t = 40 - 120$ when
 247 the simulation had reached a macroturbulent state.

270 mean zonal PV advection plays a more dominant role than nonlinear advection. In the descent
 271 region to the east of the ascent area ($0.4 < x < 1$), a negative PV tendency is caused by nonlinear
 272 advection with all other terms being negligible.

273 The dynamical balances governing the storms are very similar to that of the small-amplitude
 274 DRV mode of Kohl and O’Gorman (2022), which leads us to the conclusion that they are indeed
 275 DRVs and that the statistical equilibrium of the simulation is a DRV world. The main difference
 276 with the mode is the addition of nonlinear advection. Looking at the structure of the nonlinear
 277 advective tendency in Fig. 3d, we see that it is causing the poleward propagation that is evident
 278 in the net PV tendency and in Supplemental Video S2. Note that if we had used a basic state
 279 with westerly winds in the lower layer, the storms would propagate both eastwards and polewards.

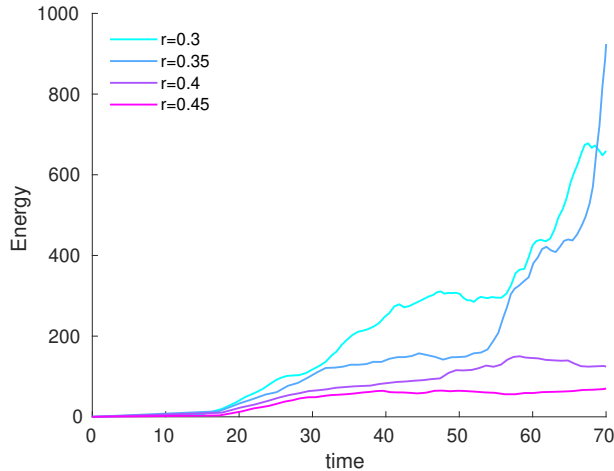


260 FIG. 4. Cross section through the PV tendencies in the lower layer shown in Fig. (3) averaged between
 261 $-0.2 < y < 0.2$. Colored lines show the PV tendency q_{2t} (blue), mean zonal advection q_{2x} (red), mean meridional
 262 advection $-v_2\bar{q}_{2y}$ (green), nonlinear advection $-J(\psi_2, q_2)$ (red dashed), diabatic generation $(1 - r(w))w$ (black),
 263 and the drag $-R\nabla^2\psi_2$ (black).

280 Poleward self advection is not found as strongly for the DRV storms observed in the current climate,
 281 which primarily have an eastward propagation (Boettcher and Wernli 2013). However, poleward
 282 propagation is found for a DRV storm identified in the warm climate regime of idealized GCM
 283 simulations (see Fig. 1 of Kohl and O’Gorman 2022). Self-advection relies on the interaction
 284 between lower and upper positive PV anomalies.⁵ We speculate that such poleward self-advection
 285 is weaker in DRVs in the current climate, because of reduced upper level negative PV anomalies
 286 as discussed in the next section.

287 Similar results for the vertical PV structure and the dynamical balances have been found by
 288 compositing on the lower-layer PV anomaly, rather than the vertical velocity, with the exception
 289 that the upper-layer negative PV anomaly is weakened compared to the lower-layer PV anomaly,
 290 and the PV tendency implies northwestward propagation instead of northward propagation (not
 291 shown).

⁵The self-advection by two opposite signed QG PV anomalies in different layers is like that of ‘hetons’ as discussed in Hogg and Stommel (1985).



293 FIG. 5. Domain mean energy of the two-layer moist QG simulations versus time for different values of r . No
 294 linear radiative damping was applied in these simulations ($\nu = 0$). Simulations below a value of $r < 0.4$ exhibit
 295 strong growth of a single vortex in the domain and a blow-up of energy over time.

292 *d. Quantifying the Transition to DRV World*

296 In this section, we seek to quantify the transition to DRV world as r is decreased and latent
 297 heating becomes stronger. One sign of a transition to vortices dominating the flow is that when the
 298 QG simulations are run without linear radiative damping ($\alpha = 0$), the simulations do not reach a
 299 statistical equilibrium for $r \lesssim 0.4$. Instead a single vortex in the domain grows rapidly to large size
 300 and become very energetic such that the domain-mean energy blows up rather than equilibrating
 301 (in practice the adaptive timestep in the solver becomes smaller and smaller, and we terminate the
 302 simulation). Fig. 5 shows the domain mean energy $\overline{(\nabla\phi)^2 + (\nabla\tau)^2 + \tau^2}$ as a function of time for a
 303 series of simulations at selected r values with $\alpha = 0$, illustrating the energy blow up for $r \lesssim 0.4$.

304 Interestingly, the energy blow-up threshold of $r \simeq 0.4$ is close to the exact threshold of $r = 0.38$
 305 below which DRV modes can exist in an infinite domain in the tilted moist two-layer model (see
 306 Fig. 6 of Kohl and O’Gorman (2022)). Thus small-amplitude modal theory seems to provide
 307 an estimate for the r value at which DRV world starts to emerge, at least as measured by the
 308 need for radiative damping to equilibrate the vortices. But it is somewhat surprising that the
 309 infinite-domain result in the tilted model (which has no basic-state PV gradients) seems to be
 310 relevant to macroturbulence with PV gradients in a finite domain. When Kohl and O’Gorman
 311 (2022) analyzed the moist instability in a finite domain with basic-state PV gradients, there was

312 no obvious threshold from wave to vortex modes at $r = 0.4$ (see Fig. 9a in Kohl and O’Gorman
 313 (2022)). However, it is possible that the finite amplitude vortices are different from the modes in
 314 this regard because meridional PV advection plays less of a role for the finite amplitude vortices
 315 considered here compared to small-amplitude modes. This could make the fully tilted model –
 316 without PV gradients – a better analogy for the fully turbulent simulations. The question of why
 317 the infinite-domain result is relevant remains open.

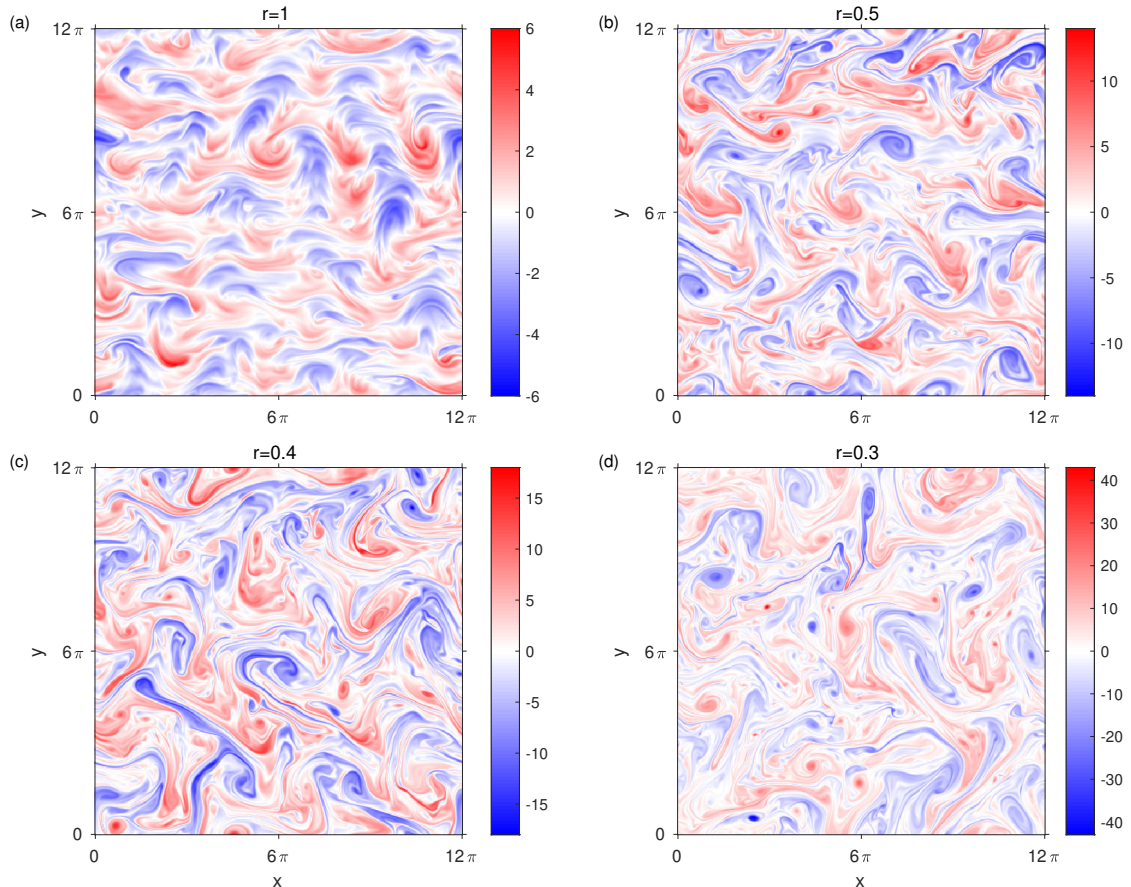
321 To further quantify the transition to DRV world, we have performed a second set of simulations
 322 using a constant radiative forcing rate $\alpha = 0.15$ spanning values of $r = 0.3 - 1$. The simulations
 323 are run until $t = 250$ and outputted every $\Delta t = 2$ times. The aim here is quantify the emergence of
 324 DRV world without the complicating factor of increases in the minimum required α for statistical
 325 equilibration as r is lowered. Snapshots of the resulting relative vorticity field in the upper layer
 326 are shown in Fig. 6 for a select number of r values. Note that for the value of α used here an
 327 equilibrated state would not be reached for r less than 0.3, and that the flow at $r = 1$ appears to
 328 be somewhat over damped. As r is lowered the flow field becomes increasingly populated by
 329 small-scale vortices (Fig. 6).

330 We quantify the transition to DRV world by introducing a metric \mathcal{M} that is inspired by our
 331 PV-based understanding of the growth of DRVs:

$$\mathcal{M} = \frac{\max((q_1 \dot{q}_1 + q_2 \dot{q}_2)^2)}{\max((q_1^2 + q_2^2)^2)} \quad (9)$$

$$(10)$$

335 where q_i are the PV anomalies in each layer, and \dot{q}_i are the PV tendencies from latent heating in
 336 each layer. The maximum functions are taken as a spatial maximum for each snapshot, and the
 337 maximum could be at different locations for different maxima in the definition. \mathcal{M} measures the
 338 collocation of PV anomalies with diabatic PV generation of the same sign which is a hallmark of
 339 latent-heating driven storms. The metric is normalized in such a way that it can be interpreted as a
 340 growth rate of moist storms, and we refer to it as the moist growth rate metric. For each simulation,
 341 the metric was calculated between $t = 100 - 250$ in the turbulent phase of the simulation and then
 342 averaged in time. The results are shown in Fig. 7b as a function of r . The moist growth rate
 343 metric increases exponentially as r is reduced with a marked increase for $r < 0.5$ (Fig. 7c), and

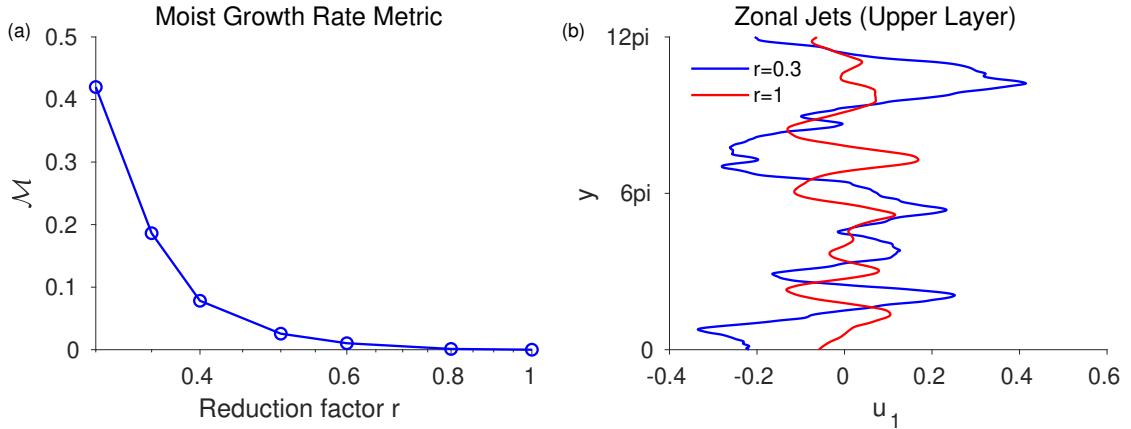


318 FIG. 6. Snapshots of the relative vorticity in the upper layer of the moist QG simulations for (a) $r = 1$, (b)
 319 $r = 0.5$, (c) $r = 0.4$, and (d) $r = 0.3$. All simulations shown were run with the same radiative damping rate of
 320 $\alpha = 0.15$. As r is lowered, the flow becomes increasingly dominated by small-scale vortices.

344 the increase is much more rapid than implied by “Clausius-Clapeyron scaling” (i.e., the increase in
 345 latent heating from reducing r at fixed w which would imply $\mathcal{M} \sim (1 - r)^2$). Taken together,
 346 the moist growth metric versus r and the equilibration behavior of the simulations without radiative
 347 damping suggest that DRV world begins to emerge at approximately $r = 0.4$.

348 Fig. 7a shows the zonal- and time-mean zonal wind averaged over $t = 100 - 250$.⁶ As r is
 349 lowered, we find that the jet spacing widens. Even though the flow field is dominated by vortices
 350 at $r = 0.3$, we see that there are still jets present (Fig. 7a). However, in the simulation run at
 351 $r = 0.01$ the jets have completely vanished (Fig. 1). However, the simulation at $r = 0.01$ has to
 352 be run with a much stronger radiative damping ($\alpha = 1.7$ instead of $\alpha = 0.15$) to reach statistical

⁶Experimenting with different averaging times, we note that while the jet positions are fairly stable at $r = 1$, they are less so at $r = 0.3$ and the jet position moves meridionally over time.



332 FIG. 7. Quantifying the transition to DRV world in QG simulations with fixed radiative damping of $\alpha = 0.15$:
 333 (a) the time-mean moist growth rate metric \mathcal{M} as a function of r , (b) zonal- and time-mean zonal wind in the
 334 upper layer for $r = 0.3$ (blue) and $r = 1.0$ (red). For both (a) and (b), time averaging was over $t = 100 - 250$.

353 equilibrium. Thus while it seems likely that the full disappearance of the jets at $r = 0.01$ is due to
 354 an even stronger vortex regime, we cannot rule out that it is caused by stronger radiative damping.

355 3. DRVs in Turbulent Simulations of Moist Primitive Equation

356 We now investigate strong diabatic storms in a set of more realistic simulations using the moist
 357 primitive equations. After nondimensionalization, the governing parameter that will be investigated
 358 is the Rossby number. Switching between high and low Rossby number regimes, while maintaining
 359 strong latent heating, will allow us to investigate the role of higher order terms in the PV dynamics
 360 beyond QG.

361 a. Model Formulation

362 The moist primitive equations in Boussinesq form, with constant planetary vorticity, r
 363 parametrization for latent heating, and Newtonian relaxation of temperature take the form

$$\frac{D\mathbf{u}}{Dt} + \mu_u \nabla^4 \mathbf{u} + f_0 \mathbf{k} \times \mathbf{u} = -\nabla \phi - R \mathbf{u}, \quad (11)$$

$$\frac{D\theta}{Dt} + \mu_\theta \nabla^4 \theta = (1-r)w\theta_z - \alpha(\theta - \theta_r), \quad (12)$$

$$u_x + v_y + w_z = 0, \quad (13)$$

$$\frac{g}{\theta_0} \theta = \phi_z, \quad (14)$$

$$\frac{D}{Dt} = \partial_t + u\partial_x + v\partial_y + w\partial_z, \quad (15)$$

$$\theta_r = \frac{z\theta_0 N^2}{g} - \frac{\theta_0 f_0 U}{g H} y, \quad (16)$$

364 where $\mathbf{u} = (u, v)$ is the horizontal velocity field, w is the vertical velocity field, ∇ is the horizontal
 365 gradient, ϕ is the geopotential height, θ is the potential temperature, θ_0 is the reference potential
 366 temperature, $\theta_r(y, z)$ is a zonally uniform reference state that is constant in time, f_0 is the constant
 367 Coriolis parameter, $r(w)$ is the nonlinear reduction factor, α is a radiative relaxation constant, g is
 368 the gravitational constant, H is the tropospheric height, U/H is the shear implied by thermal wind
 369 for the reference θ_r profile, N is a constant static stability, L_y is the domain length in the meridional
 370 direction, R is a drag coefficient, and (μ_u, μ_θ) are coefficients for horizontal hyperdiffusion.

371 The equations are being forced by relaxing θ at a rate α to a reference state θ_r with a constant
 372 static stability and a linear temperature variation in the meridional direction. In the vertical, the
 373 domain is bounded by vertical plates at $z = 0, H$ with boundary condition $w = 0$, where H now
 374 represents the full tropospheric depth. Linear drag and small-scale dissipation are applied in the
 375 momentum equations. We have found it helpful to use a drag that is constant throughout the
 376 troposphere (rather than confined to the lower levels) to prevent the build up of small-scale vertical
 377 velocities in the upper levels particularly at high Rossby number. This build up may be due to
 378 spurious wave reflections at the boundary, and for simplicity we use a vertically constant drag for
 379 all simulations.

380 The β term is neglected here, since it was found to be negligible in the QG simulations and it
 381 would introduce a term linear in y in the momentum equations that cannot be represented by the
 382 doubly-periodic Dedalus solver (Burns et al. 2020).

383 We make the model variables statistically homogeneous in the horizontal by considering the
 384 deviation θ' from the reference temperature, such that

$$\theta = \theta_r(y, z) + \theta'(x, y, z, t). \quad (17)$$

385 Similarly for geopotential, we define

$$\phi = \phi_r(y, z) + \phi'(x, y, z, t), \quad (18)$$

386 where

$$\phi_r = z^2 N^2 / 2 - f_0 (U/H) y z. \quad (19)$$

387 Plugging these decompositions into Eqs.11-15 leaves us with

$$\frac{D\mathbf{u}}{Dt} + \mu_u \nabla^4 \mathbf{u} + f_0 \mathbf{k} \times \mathbf{u} = -\nabla \phi_r - \nabla \phi' - R \mathbf{u}, \quad (20)$$

$$\frac{D\theta'}{Dt} + v\theta_{r,y} + w\theta_{r,z} + \mu_\theta \nabla^4 \theta' = (1-r)w\theta_{r,z} + (1-r)w\theta'_z - \alpha\theta', \quad (21)$$

$$u_x + v_y + w_z = 0, \quad (22)$$

$$\frac{g}{\theta_0} \theta' = \phi'_z, \quad (23)$$

$$\frac{D}{Dt} = \partial_t + u\partial_x + v\partial_y + w\partial_z, \quad (24)$$

388 Next, we nondimensionalize the equations using QG scaling (but keeping all terms) such that $x, y \sim$
 389 L_D with deformation radius⁷, $L_D = NH/f_0$, $z \sim H$, $t \sim L_D/U$, $\mathbf{u}, \mathbf{v} \sim U$, $w \sim \epsilon UH/L_D$ where $\epsilon =$
 390 U/f_0L_D is the Rossby number, $\phi' \sim f_0UL_D$, $\theta' \sim \theta_0 f_0UL_D/gH$ to obtain the nondimensionalized
 391 equations

⁷The definition of the deformation radius is different here from the QG system discussed in section 2 because H now refers to the full tropospheric height, and we have dropped the $\sqrt{2}$. We will see from the numerical simulations that scaling the length scale like the deformation radius remains a reasonable choice for the PV anomalies even in the presence of strong latent heating. In the DRV modal theory of Kohl and O’Gorman (2022), the ascent length scale vanishes as $r \rightarrow 0$, but the PV anomaly in the descent area is sustained by a balance of growth and zonal advection leading to an exponential decay length L_D/σ where σ is the growth rate. But since the growth rate approaches $\sigma = 1.62$ in the limit of $r \rightarrow 0$, the length scale of the PV disturbance also remains finite in this limit, at roughly $0.62L_D$ which is close to L_D .

$$\epsilon \frac{D\mathbf{u}}{Dt} + \widetilde{\mu}_u \nabla^4 \mathbf{u} + \mathbf{k} \times \mathbf{u} = z \mathbf{e}_y - \nabla \phi' - \widetilde{R} \mathbf{u}, \quad (25)$$

$$\frac{D\theta'}{Dt} - v + w + \widetilde{\mu}_\theta \nabla^4 \theta' = (1-r)w + \epsilon(1-r)w\theta'_z - \widetilde{\alpha}\theta', \quad (26)$$

$$u_x + v_y + \epsilon w_z = 0, \quad (27)$$

$$\theta' = \phi'_z, \quad (28)$$

$$\frac{D}{Dt} = \partial_t + u\partial_x + v\partial_y + \epsilon w\partial_z, \quad (29)$$

392 with nondimensional numbers $\epsilon = \frac{U}{f_0 L_D} = \frac{U}{NH}$, $\widetilde{R} = \frac{1}{f_0} R$, $\widetilde{\alpha} = \frac{L_D}{U} \alpha$, $\widetilde{L}_y = \frac{1}{L_D} L_y$, $\widetilde{\mu}_u = \frac{1}{f_0 L_D^4} \mu_u$, and
 393 $\widetilde{\mu}_\theta = \frac{1}{U L_D^3} \mu_\theta$ and unit vector in the meridional direction \mathbf{e}_y .

394 We note that as a result of scaling horizontal length scales with the deformation radius, what
 395 we refer to as the Rossby number in these simulations $\epsilon = \frac{U}{f_0 L_D}$ could also be interpreted as the
 396 Froude number $\frac{U}{NH}$ or the inverse square root of the Richardson number $\frac{N^2 H^2}{U^2}$. We stick to the
 397 designation of Rossby number here to reflect the intuition that a low Rossby number limit recovers
 398 quasigeostrophic dynamics. Furthermore, we note that in the definition of the Rossby number U/H
 399 should be interpreted as the mean-state zonal wind shear (rather than, say, the local wind shear
 400 in a storm) and as such $\epsilon = U/NH$ refers to a mean-state Rossby number rather than the Rossby
 401 number of an individual storm (which could be much higher).

402 The equations are solved using a spectral solver with adaptive time stepping (Burns et al. 2020)
 403 on a doubly periodic square domain of side $\widetilde{L}_y = 6\pi$, with horizontal plates at $z = 0$ and $z = 1$ and
 404 $128 \times 128 \times 10$ grid points. Chebyshev polynomials are used as basis functions in the vertical (the
 405 grid spacing between the 10 vertical levels is close to uniform in the interior but slightly smaller
 406 towards the boundaries). The simulations are initialized with random conditions for all fields, after
 407 filtering out all wavenumbers with $k = \sqrt{k_x^2 + k_y^2} > 3$ to avoid having to integrate a lot of small scale
 408 noise in the initial phase of the simulation. The simulations are run until $t = 160$ and outputted
 409 every $\Delta t = 0.5$.

410 We run simulations with a high Rossby number $\epsilon = 0.4$, an intermediate Rossby number $\epsilon = 0.1$,
 411 and a low Rossby number $\epsilon = 0.01$ while keeping the latent heating strong at $r = 0.01$ in all
 412 cases. For reference, using typical scales $U = 10 \text{ m s}^{-1}$, $L_D = 1000 \text{ km}$ and $f_0 = 10^{-4} \text{ s}^{-1}$ and so
 413 the intermediate Rossby number $\epsilon = U/f_0 L_D = 0.1$ is closest to typical Earth-like conditions. The

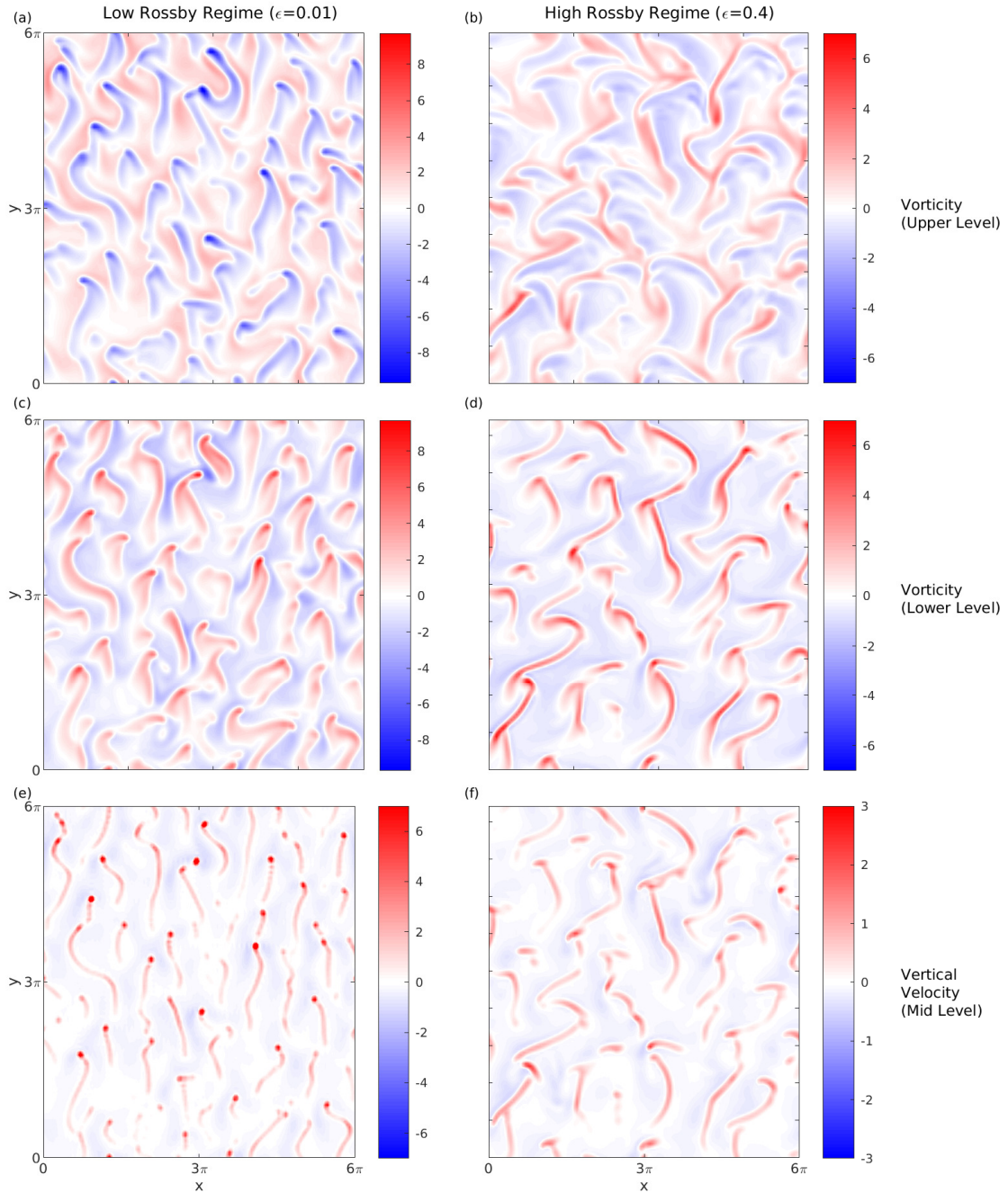
414 drag coefficient and momentum hyperdiffusion coefficient need to be smaller in the intermediate
 415 and low Rossby regime so that the ratios \tilde{R}/ϵ and $\tilde{\mu}_u/\epsilon$ remain approximately constant and the QG
 416 limit is properly recovered as ϵ tends to zero. For the high Rossby number run, we choose $\tilde{R} = 0.11$
 417 and $\tilde{\mu}_u = 5 \times 10^{-5}$, for the intermediate Rossby number run $\tilde{R} = 2.75 \times 10^{-2}$ and $\tilde{\mu}_u = 1.25 \times 10^{-5}$,
 418 and the low Rossby number run $\tilde{R} = 2.75 \times 10^{-3}$ and $\tilde{\mu}_u = 1.25 \times 10^{-6}$.

419 The hyperdiffusion for temperature is $\mu_\theta = 5 \times 10^{-5}$ in all cases. The radiative relaxation co-
 420 efficient was chosen to be $\alpha = 0.35$ for the high Rossby number simulation and $\alpha = 0.6$ for the
 421 intermediate and low Rossby number simulations. A higher relaxation coefficient was found to be
 422 necessary at intermediate and low Rossby numbers in order to stabilize the simulations. As we will
 423 see in the next section, while the simulations at intermediate and low Rossby number transition to
 424 DRV world similar to the QG simulations, the simulation at high Rossby number does not transi-
 425 tion to a DRV world. The need for a stronger relaxation with onset of the vortex regime is hence
 426 consistent with what was found for the QG simulations in which radiative damping was needed
 427 for equilibration when a DRV world emerged. We also explored primitive-equation simulations
 428 in which the background temperature gradient was not imposed but rather the temperature was
 429 relaxed to a cosinusoidal reference temperature. Thus, the radiative forcing is not as strong, and it
 430 is easier for the flow to equilibrate. Note that the cosinusoidal reference temperature was chosen
 431 because relaxation to a linear gradient is not possible in a doubly periodic solver. In this case we
 432 found that it is possible to run the simulations with the same relaxation coefficient for all Rossby
 433 numbers. Transition to DRV world at low Rossby number persists and the structure of storms is
 434 similar to what we present in the next section. We stick to the linear temperature gradient set-up
 435 here because its interpretation is simpler, and it makes a closer connection to the QG simulations
 436 discussed previously in section 2.

437 *b. Simulation Results*

444 Fig. 8 shows snapshots of the relative vorticity at a lower level ($z = 0.15$) and an upper level
 445 ($z = 0.85$), and the vertical velocity around mid-level ($z = 0.42$) in the macroturbulent phase of the
 446 simulations for the low and high Rossby number simulations.

447 In the low Rossby number simulation (Fig. 8 b,d,f), the character of the flow is dramatically
 448 different from that in Earth's midlatitude atmosphere. The flow field is not wave-like and is



438 FIG. 8. Snapshots of the relative vorticity at a lower ($z = 0.15$) and upper level ($z = 0.85$) and vertical velocity
 439 ($z = 0.42$) around mid-level for (a,c,e) a low Rossby number simulation ($\epsilon = 0.01$), and (b,d,f) a high Rossby
 440 number simulation ($\epsilon = 0.4$) run in the moist primitive equation simulations at $r = 0.01$. At low Rossby number,
 441 the flow is a DRV world with vorticity dipoles that propagate poleward. At high Rossby number, the poleward
 442 propagation is slower and the flow has both vortices and fronts. Animations of the two simulations can be found
 443 in Supplemental Videos S3 and S4.

449 disrupted by vorticity dipoles, positive in the lower layer and negative in the upper layer of roughly
 450 equal strength. The vorticity dipoles continuously spawn and rapidly propagate poleward as can
 451 be most clearly seen in Supplemental Video S3. Similarly, the vertical velocity field breaks up
 452 into isolated vertical velocity maxima, associated with the vorticity dipoles, and is characterized
 453 by a large vertical-velocity asymmetry parameter $\lambda = 0.88$. The simulation is clearly a DRV world
 454 similar to the strong latent heating regime of the moist QG simulations.

455 In the high Rossby number simulation (Fig. 8 a,c,e), by contrast, the vorticity in the upper
 456 troposphere is more wave-like and larger in scale. In the lower-troposphere, there are still smaller-
 457 scale vortices but these are now associated with prominent frontal bands. The vorticity field is
 458 stronger in the lower troposphere compared to the upper troposphere. The storms evolve more
 459 slowly, and while they still drift poleward, their primary propagation is eastward, as can be seen
 460 in Supplemental Video S4. The vertical velocity field is made up of frontal bands and localized
 461 maxima, resembling the midlatitude vertical velocity field in Earth's atmosphere. The vertical
 462 velocity asymmetry parameter is $\lambda = 0.75$ which is similar to what was found in the reduced
 463 stability GCM simulations of O'Gorman et al. (2018) at $r = 0.01$. The flow does not show signs of
 464 transition to a purely vortex dominated regime despite the strong latent heating.

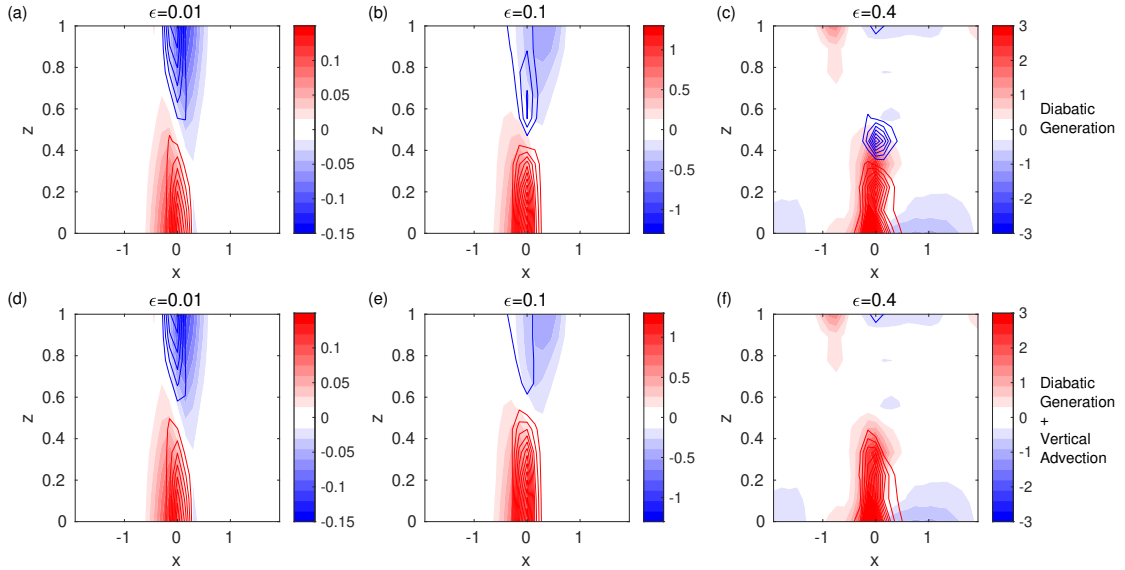
465 In the intermediate Rossby number simulation (Supplemental Video 5), the flow is vortex
 466 dominated, and we consider it to be still a DRV world. A stream of vortices that continuously
 467 spawn and quickly propagate poleward can be clearly seen. However, the flow also retains some
 468 frontal features that were observed in the high Rossby number simulation. We conclude that the
 469 transition to a DRV world with decreasing Rossby number is gradual rather than abrupt.

470 Next we turn to the PV structure of the storms for the high and low Rossby number simulations.
 471 We calculate the Ertel PV

$$Q = (1 + \epsilon\zeta)\theta_z - \epsilon^2 v_z \theta_x + \epsilon^2 u_z \theta_y, \quad (30)$$

472 where $\zeta = v_x - u_y$ and $\theta_z = 1 + \epsilon\theta'_z$, and subtract the zonal mean to define the PV anomalies. We
 473 also calculate the PV tendency from latent heating

$$\dot{Q}_{\text{LH}} = \epsilon(1 + \epsilon\zeta)\dot{\theta}'_z, \quad (31)$$



479 FIG. 9. Storm composite of Ertel PV anomaly (shading) and PV tendency from latent heating (contours)
 480 for (a) the low Rossby number simulation ($\epsilon = 0.01$), (b) the intermediate Rossby number simulation ($\epsilon = 0.1$)
 481 and (c) the high Rossby number simulation ($\epsilon = 0.4$). The contour interval is (a,d) 0.1, (b,e) 0.5 and (c,f) 2.1.
 482 The zero contour line for the PV tendencies is not shown. Panels (d,e,f) show the same storm composites for
 483 the low, intermediate, and high Rossby number simulation as in (a,b,c) but now the PV tendency includes the
 484 contributions from latent heating plus vertical advection. Composite means were made over the 10 strongest
 485 vertical velocity maxima at each output time between $t = 70 - 160$.

474 where $\dot{\theta} = [(1 - r(w))w\theta_z]$, and we have ignored contributions due to horizontal gradients of the
 475 heating profile. Equations 30 and 31 are derived in section a of the appendix. We then composite
 476 PV anomalies and PV tendencies over the 10 strongest vertical velocity maxima at each simulation
 477 output between $t = 70 - 160$ when the simulations are in statistical equilibrium. The results are
 478 shown in Figure 9 a,b,c for the low, intermediate and high Rossby number simulations.

486 While the low Rossby number storms show a clear dipole structure both in terms of PV anomaly
 487 and PV tendency, the high Rossby number storms are made up of a strong low level positive PV
 488 anomaly only (Fig. 9,c). No strong negative PV anomaly is visible at the location of negative
 489 diabatic PV generation, although a weaker positive and negative PV anomaly signal is visible at
 490 the top boundary. Negative diabatic generation is weaker compared to positive diabatic generation.
 491 For the intermediate Rossby number regime, a clear negative PV anomaly is visible at the location
 492 of negative diabatic generation (Fig. 9b). Unlike in the low Rossby number case, at intermediate

493 Rossby numbers the negative PV anomaly aloft is weaker compared to the low level positive
494 anomaly. While diabatic generation extends over the entire vertical extent of the domain at low
495 and intermediate Rossby number, diabatic generation remains mostly confined to the lower part of
496 the domain at high Rossby number. Overall, Fig. 9a-c shows the weakening of upper level PV
497 anomaly and diabatic generation as the Rossby number is increased.

498 If vertical PV advection $-\epsilon w Q_z$ is added to the PV tendency from latent heating (cf. Appendix
499 a for derivation), the negative PV generation in the high Rossby number composite at $z = 0.5$ is
500 almost entirely cancelled, with a weaker signal persisting at the upper boundary (Fig. 9f). By
501 contrast, negative generation persists for the low and intermediate Rossby number storms (Fig.
502 9d,e).

503 The PV structure of the low Rossby number storm resembles that of the small-amplitude DRV
504 mode from theory (Fig. 3 in Kohl and O’Gorman 2022), while the PV structure of the high Rossby
505 number storm resemble that of DRVs from reanalysis in the current climate (Fig. 10 in Kohl and
506 O’Gorman 2022). The Rossby number is low for small-amplitude modes and high for storms in
507 reanalysis, and hence the similarity between the low Rossby numbers storms and DRV modes, and
508 between the high Rossby number storms and DRV storms in reanalysis is as expected.

509 *c. Discussion*

510 The primitive-equation simulations with strong latent heating show that changes in the Rossby
511 number bring about important changes both in terms of the PV structure of individual storms and
512 in terms of the overall circulation. In particular, low Rossby numbers make the simulations more
513 like DRV world in which diabatically maintained PV dipoles continuously spawn and propagate
514 poleward. At higher Rossby number, DRVs still occur but they have a different PV structure, they
515 do not propagate as quickly poleward and they do not fully dominate the flow which now also
516 includes frontal features.

517 We note that for the high Rossby number storms (Fig. 9c), a weak positive PV anomaly at
518 upper levels is visible westward of the strong low level positive PV anomaly, unlike in the low
519 and intermediate Rossby number storms. This upper-level positive PV anomaly suggests that at
520 high Rossby number there may be some growth induced from a type-C cyclogenesis mechanism
521 as found in Ahmadi-Givi et al. (2004). We leave exploration of this to future work.

522 4. Toy Model for the Vertical Structure of PV in Finite Amplitude DRVs

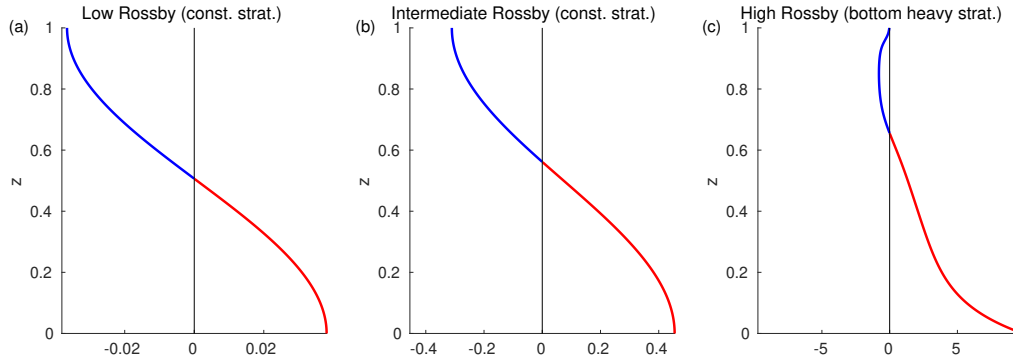
523 We study a 1-D toy model for the vertical structure of PV in the ascent region of a DRV in order
 524 to understand why the PV structure is different at high versus low Rossby number. This model
 525 will also help to bridge the gap between the theory of DRV modes and finite-amplitude storms,
 526 although we emphasize that it is not a full model because the vertical velocity profile w will be
 527 taken as given. This approach is similar to previous studies of the PV evolution given prescribed
 528 vertical velocity or heating profiles (Schubert and Alworth 1987; Abbott and O’Gorman 2024).
 529 The model equations are the thermodynamic equation with reduced stability parameterization of
 530 latent heating and the PV evolution equation:

$$\partial_t \theta' + w \bar{\theta}_z + \epsilon w \theta'_z = \dot{\theta}, \quad (32)$$

$$\partial_t Q = \epsilon \frac{Q \dot{\theta}_z}{\bar{\theta}_z + \epsilon \theta_z} - \epsilon w Q_z, \quad (33)$$

531 where $\bar{\theta}_z$ represents a background stratification that is assumed constant in time, and $\dot{\theta} = (1 -$
 532 $r)w\bar{\theta}_z + \epsilon(1 - r)w\theta'_z$ is the latent heating rate. We focus on a single vertical column ($0 \leq z \leq 1$)
 533 in a region of maximum heating in the horizontal such that $\dot{\theta}_x = \dot{\theta}_y = 0$, approximate the PV as
 534 $Q = (1 + \epsilon \zeta) \theta_z$, which ignores the terms $\epsilon^2 v_z \theta_x$ and $\epsilon^2 u_z \theta_y$, and ignore any horizontal PV transport.
 535 A derivation is given in section b of the appendix. The toy model is evolved forward in time for a
 536 high ($\epsilon = 0.4$), intermediate ($\epsilon = 0.1$) and low Rossby number ($\epsilon = 0.01$) with the aim of matching
 537 the storms found in the moist primitive equation simulations (Fig. 9). The integration is started
 538 from the initial conditions $\theta' = 0$ and $Q = \bar{\theta}_z$. For the low and intermediate Rossby number we
 539 choose a constant background stratification $\bar{\theta}_z = 1$ and for the high Rossby number we choose a
 540 bottom-heavy stratification $\bar{\theta}_z = 1 + 0.25 e^{-(z-0.2)/0.1}$, since that is what was found for the storms
 541 in the simulations (not shown). The bottom-heavy stratification leads to bottom-amplified heating
 542 rates, per the r parameterization of latent heating. The vertical velocity profile is fixed in time as
 543 $w = \sin(\pi z)$ which is symmetric about $z = 0.5$. A vertically constant profile is again chosen for r
 544 with a value of $r = 0.01$.

550 The equations are evolved forward in time until $t = 1.2$, which corresponds roughly to $t =$
 551 $1.2L_D/U = 33\text{h}$ using typical scales $L_D = 1000\text{km}$ and $U = 10\text{m s}^{-1}$. The resulting PV anomaly



545 FIG. 10. PV anomaly profiles produced by the toy-model Eqs. (32-33) at $t = 0.5$ using a value of $r = 0.01$
 546 for (a) a low Rossby number storm of $\epsilon = 0.01$, (b) an intermediate Rossby number storm of $\epsilon = 0.1$, and (c) a
 547 high Rossby number storm of $\epsilon = 0.4$. For the low and intermediate Rossby number storms we use a constant
 548 background stratification, but for the high Rossby number storm we use a bottom-heavy stratification. The PV
 549 anomalies are defined with respect to the initial conditions.

552 profiles are shown in Fig. 10 where we have defined PV anomalies with respect to the initial PV
 553 profile.

554 We focus first on the low Rossby number case (Fig. 10a). The PV profile has the typical dipole
 555 structure seen in the moist QG storms (Fig. 2), low-Rossby number storms of the moist primitive
 556 equation simulations (Fig. 9a), and the DRV modes from theory (Kohl and O’Gorman 2022). The
 557 PV is antisymmetric about the altitude of maximum ascent $z = 0.5$. By contrast, the intermediate
 558 Rossby number case which also has a constant background stratification has stronger positive than
 559 negative PV anomalies (Fig. 10b) and its structure bears close resemblance to the storms found in
 560 the moist primitive equation simulations at intermediate Rossby number (Fig. 9b). The different
 561 magnitude of positive and negative PV anomalies arises because of the appearance of the PV in
 562 the diabatic generation term – the first term on the right-hand side of Eq. (33) – which amplifies
 563 the generation of positive PV anomalies but weakens the generation of negative PV anomalies,
 564 leading to a nonlinear feedback as the PV anomalies evolve. For the low Rossby number case, this
 565 feedback is negligible because the PV anomalies are too weak to strongly affect the PV and thus
 566 too weak to affect the diabatic PV production, but for the intermediate Rossby number case the
 567 feedback is important because the PV anomalies are larger. We also note that in Fig. 10b, vertical
 568 advection – the second term on the right-hand side of Eq. (33) – has begun to move the positive
 569 PV anomaly upwards so that the change from positive to negative PV anomaly no longer occurs at

570 about $z = 0.5$ but instead at $z = 0.56$. If the time integration is continued, the positive PV anomaly
571 would keep being advected vertically and gradually begin to fill up the entire vertical column until
572 no negative PV anomaly is left (not shown). This limit is spurious however, since the assumption
573 of a sustained vertical velocity profile would break down.

574 Looking at the high Rossby number case with bottom-heavy background stratification (Fig. 10c),
575 we notice that the positive PV anomaly has grown even larger than for the intermediate Rossby
576 number case. The PV structure is highly asymmetric in magnitude between positive and negative
577 PV anomalies with the surface PV anomaly about 12 times stronger than the negative PV anomaly
578 aloft. This is because the positive PV generation is larger at high Rossby number, and also because
579 the bottom heavy stratification implies a bottom heavy heating rate. The vertical gradient of
580 the heating rate, which affect the diabatic PV generation, is larger below the heating maximum,
581 leading to stronger positive generation, and weaker above the heating maximum, leading to weaker
582 negative PV generation. This signal then gets amplified by the nonlinear feedback between PV
583 and the heating gradient leading to highly asymmetric bottom heavy storms as were found in the
584 high Rossby number moist primitive equation simulations (Fig. 9c). If we consider high Rossby
585 number but vertically constant background stratification, the asymmetry in PV structure is still
586 substantial but not quite as large: the surface positive PV anomaly is about 4.5 times stronger than
587 the negative PV anomaly aloft

588 Due to the nonlinearity of the feedback between PV anomalies and diabatic PV generation, the
589 strength of the low-level PV anomaly that is reached at the end of the integration is very sensitive
590 to the magnitude of the Rossby number, the bottom-heaviness of the heating rate and the time
591 over which the heating acts (here given by the integration time). For the high Rossby number
592 storm, doubling of the Rossby number to $\epsilon = 0.8$ leads to a surface PV anomaly that is about 5
593 times larger (not shown). This sensitive dependence of the PV asymmetry on the Rossby number
594 and the bottom-heaviness of the heating profile explains the differences found between the PV
595 structure of the winter and summer DRV example discussed in Kohl and O’Gorman (2022). In
596 that case, the winter storm was found to be more asymmetric in terms of the magnitude of positive
597 versus negative PV anomalies (no clear negative PV identifiable) because it was a stronger storm,
598 implying a higher Rossby number, with a more bottom-heavy diabatic heating profile.

599 5. Conclusions

600 Finite amplitude effects in DRVs were explored in simulations of moist macroturbulence using
601 the QG and primitive equations, and an attempt was made at synthesis in the form of a toy model
602 of the vertical structure of PV.

603 Moist QG simulations with a reduced stability parametrization transition from a state of wavy jets
604 interspersed with vortices to a vortex dominated state (DRV world) as latent heating is increased.
605 PV budget analysis revealed that the vortices in the strong latent heating regime are DRVs with
606 diabatic generation dominating over meridional PV advection. The solutions are maintained by
607 a balance between mean zonal advection, nonlinear advection and diabatic generation. This is
608 very similar to the balances maintaining the small-amplitude DRV mode from theory, with the
609 additional effect of nonlinear advection which leads to poleward self advection. DRV world begins
610 to emerge at about $r = 0.4$, which is similar to the condition of $r < 0.38$ for DRV modes to exist on
611 an infinite domain (Kohl and O’Gorman 2024). One piece of evidence that DRV world is starting to
612 emerge near $r = 0.4$ is that simulations run without radiative damping fail to equilibrate for $r \lesssim 0.4$
613 due to explosive growth of a single vortex in the domain. We also quantified the transition to DRV
614 world using a moist growth-rate metric that measures collocation of PV anomalies with diabatic
615 PV generation of the same sign, and this showed a rapid pickup near $r = 0.4$. It would be interesting
616 to generalize and test this metric for storms in more realistic simulations and observations in future
617 work.

618 Multilevel simulations of the moist primitive equations in a doubly periodic configuration were
619 run for a low, intermediate (closest to earth-like conditions) and high Rossby number regimes
620 while keeping latent heating strong. The simulations show that changes in the Rossby number
621 cause important changes in the overall macroturbulent flow and the PV structure of strong diabatic
622 storms. At low Rossby number the zonal flow becomes disrupted by isolated vorticity dipoles
623 which continuously spawned and self-advected poleward. The vertical velocity field breaks up
624 into isolated maxima with a strong asymmetry between upward and downward motion. At high
625 Rossby number the flow maintains a wave-like structure in the upper troposphere, and there are
626 a mix of DRV-like storms and frontal features such that there is not a pure DRV world. The
627 storms primarily propagate eastward although still with some weaker poleward propagation. In the
628 intermediate Rossby number regime, rapidly poleward propagating vortices emerged as in the low

629 Rossby number regime. However, the flow also retained some frontal features that were observed
630 in the high Rossby number regime. We conclude from this that the transition to DRV world with
631 decreasing Rossby number appears to be gradual rather than abrupt. While the PV structure of
632 strong diabatic storms in the low and intermediate Rossby number simulations resembles that of
633 the QG DRV storms and DRV modes, the PV structure of storms in the high Rossby number
634 simulations are more asymmetric and bottom confined and resembled that of DRVs observed in
635 the current climate. We conclude that higher order terms in the PV dynamics beyond QG play an
636 important role in setting the structure of storms, their propagation, and the extent to which the flow
637 is dominated by DRVs.

638 Finite amplitude effects beyond the small-amplitude QG DRV theory were further explored
639 within a simple toy model of the moist thermodynamic and PV equations in a single ascending
640 column. The toy model was solved for a low, intermediate and a high Rossby number and found to
641 reproduce much of the variety of storm structure found in the moist primitive equation simulations.
642 For low Rossby numbers the diabatic PV tendency behaves like the vertical gradient of the latent
643 heating profile (cf. Eq. 31). If the profile is symmetric this will lead to generation of positive and
644 negative PV anomalies of equal magnitude, as was found for DRV storms in QG simulations and
645 primitive equation simulations at small Rossby number. When the Rossby number is increased,
646 the PV tendency is proportional to the product of the absolute vorticity and the heating rate -
647 which amplifies the generation of positive PV anomalies but weakens the generation of negative
648 PV anomalies, leading to a nonlinear feedback as the PV anomalies evolve. This leads to PV
649 constellations where the low level positive PV anomaly is stronger than the negative PV anomaly
650 aloft as was found in moist primitive equation simulations at intermediate and high Rossby numbers.
651 In particular, it was found that when a strong Rossby number is coupled with a bottom heavy heating
652 profile, which favors larger values of positive PV generation, this can lead to a feedback which
653 rapidly generates strong low level PV anomalies with much smaller upper level negative anomaly
654 - as is often found for DRVs observed in the current climate (e.g. Wernli et al. 2002, Kohl and
655 O’Gorman 2022). Strong sensitivity of the asymmetry of the magnitude of negative versus positive
656 PV anomalies was found to the degree of bottom heaviness of the heating rate and the magnitude
657 of the Rossby number. Future work could investigate this sensitive dependence by looking at a

658 variety of realistic storm systems relating the vertical profile of heating rates to the magnitude of
659 the PV anomalies.

660 Given that a negative PV anomaly is required for diabatic growth and poleward self-advection,
661 the results lead us to the following speculation. In the current climate, where heating rates are more
662 bottom heavy, diabatic generation leads to the rapid genesis of low level positive PV anomalies.
663 The negative PV anomaly is quickly eroded away (or at least does not grow as quickly as the positive
664 PV anomaly) limiting diabatic growth and poleward self advection. Meanwhile the diabatically
665 generated positive PV anomaly has become sufficiently large in amplitude to be able to undergo
666 nonlinear interaction with upper level PV anomalies in a later secondary growth process (Wernli
667 et al. 2002).

668 The Rossby number in our simulations is given by $\epsilon = U/f_0L_D = U/NH$ where U/H should be
669 interpreted as the mean-state zonal wind shear (rather than, say, the local wind shear in a storm).
670 Hence, smaller Rossby numbers could be achieved by weaker mean zonal shear or stronger static
671 stability N , both of which could occur at least regionally in a warming midlatitude climate. Future
672 work could investigate the extent to which there is a transition to a more vortex dominated flow
673 (or even a full DRV world) in GCMs in warm and moist climates when the Rossby number is low,
674 e.g. by varying the strength of the midlatitude jet. This could confirm whether the tendency for a
675 more vortex dominated flow to occur at low Rossby number and with strong latent heating holds
676 in models with a more realistic representation of moist physics.

677 *Acknowledgments.* We acknowledge helpful discussions with Santiago Benavides, Andre da Silva,
 678 Minmin Fu, Keaton Burns, Martín Vélez-Pardo, Stephan Pfahl, Kerry Emanuel, and Glenn Flierl.
 679 We acknowledge support from NSF AGS 2031472 and the mTerra Catalyst Fund.

680 *Data availability statement.* Model code for the moist QG and moist primitive equation simula-
 681 tions is available on github (https://github.com/matthiuekohl/DRV_World_Paper).

682 APPENDIX

683 *a. PV equation for the primitive-equation model*

684 Eqs. (11-14) can be combined into an equation for the PV Q (Vallis 2017, his Eq. 4.96)

$$\frac{DQ}{Dt} = (f_0 + \zeta)\dot{\theta}_z - v_z\dot{\theta}_x + u_z\dot{\theta}_y, \quad (\text{A1})$$

685 where

$$Q = (f_0 + \zeta)\theta_z - v_z\theta_x + u_z\theta_y, \quad (\text{A2})$$

$$\dot{\theta} = (1 - r)w\theta_z, \quad (\text{A3})$$

$$\theta_z = \bar{\theta}_z + \theta'_z, \quad (\text{A4})$$

$$\frac{D}{Dt} = \partial_t + u\partial_x + v\partial_y + w\partial_z, \quad (\text{A5})$$

686 $\bar{\theta}_z$ is a background stratification, and we have ignored the drag, relaxation and hyperdiffusion
 687 terms in Eq. (A1). Nondimensionalizing the vertical potential temperature gradients like $\theta'_z \sim$
 688 $\theta_0 f_0 U L_D / g H^2$, $\bar{\theta}_z \sim \theta_0 N^2 / g$, the PV like $Q \sim f_0 \bar{\theta}_z = f_0 \theta_0 N^2 / g$ and the rest of the variables with
 689 scales as outlined in section (3), we obtain the nondimensional PV equation

$$\frac{DQ}{Dt} = \epsilon(1 + \epsilon\zeta)\dot{\theta}_z - \epsilon^2 v_z \dot{\theta}_x + \epsilon^2 u_z \dot{\theta}_y, \quad (\text{A6})$$

690 where

$$Q = (1 + \epsilon\zeta)\theta_z - \epsilon^2 v_z \theta_x + \epsilon^2 u_z \theta_y, \quad (\text{A7})$$

$$\dot{\theta} = (1 - r)w\theta_z, \quad (\text{A8})$$

$$\theta_z = \bar{\theta}_z + \epsilon\theta'_z, \quad (\text{A9})$$

$$\frac{D}{Dt} = \partial_t + u\partial_x + v\partial_y + \epsilon w\partial_z \quad (\text{A10})$$

691 and all variables are now nondimensional. Eq. (A7) corresponds to Eq. (30) used for the PV in
 692 section (3), where in that section we use a background stratification equal to the reference state
 693 such that $\theta_z = 1 + \epsilon\theta'_z$. The first term on the rhs of Eq. (A6) corresponds to Eq. (31) used for the
 694 PV tendency from latent heating in section (3).

695 *b. Derivation of the governing equations for the 1-D toy model of vertical PV structure*

696 If we place ourselves at the location of the heating maximum $\dot{\theta}_x = \dot{\theta}_y = 0$, neglect all horizontal
 697 transport of PV, and neglect the higher order vertical shear terms in the PV, then Eqs. (A6) and
 698 (A7) simplify to

$$\partial_t Q + \epsilon w Q_z = \epsilon(1 + \epsilon\zeta)\dot{\theta}_z \quad (\text{A11})$$

$$Q = (1 + \epsilon\zeta)\theta_z, \quad (\text{A12})$$

699 which we can rewrite as

$$\partial_t Q = \epsilon \frac{Q\dot{\theta}_z}{\bar{\theta}_z + \epsilon\theta'_z} - \epsilon w Q_z, \quad (\text{A13})$$

700 which is the form of the PV equation (Eq. 33) used in the simple 1D toy-model in section (4).

701 The thermodynamic equation in the simple 1-D toy model (Eq. 32) is derived similarly to
 702 Eq. (26) but neglecting horizontal advection of perturbation θ' and reference theta (the v term),
 703 neglecting hyperdiffusion and radiative relaxation, and using $\bar{\theta}$ in place of θ_r .

704 **References**

- 705 Abbott, T. H., and P. A. O’Gorman, 2024: Impact of precipitation mass sinks on midlatitude
706 storms in idealized simulations across a wide range of climates. *Weather and Climate Dynamics*,
707 <https://doi.org/10.5194/wcd-5-17-2024>.
- 708 Ahmadi-Givi, F., G. C. Graig, and R. S. Plant, 2004: The dynamics of a midlatitude cyclone
709 with very strong latent-heat release. *Quart. J. Roy. Meteor. Soc.*, **130**, 295–323, <https://doi.org/10.1256/qj.02.226>.
- 711 Boettcher, M., and H. Wernli, 2013: A 10-yr climatology of diabatic rossby waves in the northern
712 hemisphere. *Mon. Wea. Rev.*, **141**, 1139–1154, <https://doi.org/10.1175/MWR-D-12-00012.1>.
- 713 Boettcher, M., and H. Wernli, 2015: Diabatic Rossby waves in the Southern Hemisphere. *Quarterly*
714 *Journal of the Royal Meteorological Society*, **141**, 3106–3117, <https://doi.org/10.1002/qj.2595>.
- 715 Burns, K. J., G. M. Vasil, J. S. Oishi, D. Lecoanet, and B. P. Brown, 2020: Dedalus: A flexible
716 framework for numerical simulations with spectral methods. *Physical Review Research*, **2**,
717 023 068, <https://doi.org/10.1103/PhysRevResearch.2.023068>.
- 718 Charney, J. G., 1947: The dynamics of long waves in a baroclinic westerly current. *J. Atmos. Sci.*,
719 **4**, 136–162, [https://doi.org/10.1175/1520-0469\(1947\)004<0136:tdolwi>2.0.co;2](https://doi.org/10.1175/1520-0469(1947)004<0136:tdolwi>2.0.co;2).
- 720 Davis, C. A., and K. A. Emanuel, 1991: Potential vorticity diagnostics of cyclogenesis.
721 *Monthly Weather Review*, **119**, 1929–1953, [https://doi.org/10.1175/1520-0493\(1991\)119<1929:](https://doi.org/10.1175/1520-0493(1991)119<1929:PVDOC>2.0.CO;2)
722 [PVDOC>2.0.CO;2](https://doi.org/10.1175/1520-0493(1991)119<1929:PVDOC>2.0.CO;2).
- 723 Eady, E. T., 1949: Long Waves and Cyclone Waves. *Tellus*, **1**, 33–52, [https://doi.org/10.3402/](https://doi.org/10.3402/tellusa.v1i3.8507)
724 [tellusa.v1i3.8507](https://doi.org/10.3402/tellusa.v1i3.8507).
- 725 Emanuel, K. A., M. Fantini, and A. J. Thorpe, 1987: Baroclinic instability in an environment of
726 small stability to slantwise moist convection. Part I: two-dimensional models. *J. Atmos. Sci.*, **44**,
727 1559–1573, [https://doi.org/10.1175/1520-0469\(1987\)044<1559:BIIAEO>2.0.CO;2](https://doi.org/10.1175/1520-0469(1987)044<1559:BIIAEO>2.0.CO;2).
- 728 Fantini, M., 1995: Moist Eady waves in a quasigeostrophic three-dimensional model. *J. Atmos.*
729 *Sci.*, **52**, 2473–2485.

- 730 Hogg, N., and H. Stommel, 1985: The heton, an elementary interaction between discrete baroclinic
731 geostrophic vortices, and its implications concerning eddy heat-flow. *Proceedings of the Royal*
732 *Society of London. A. Mathematical and Physical Sciences*, **397**, 1–20, [https://doi.org/10.1098/](https://doi.org/10.1098/rspa.1985.0001)
733 [rspa.1985.0001](https://doi.org/10.1098/rspa.1985.0001).
- 734 Kohl, M., and P. A. O’Gorman, 2022: The Diabatic Rossby Vortex: Growth Rate, Length Scale
735 and the Wave-Vortex Transition. *J. Atmos. Sci.*, **79**, 2739–2755.
- 736 Kohl, M., and P. A. O’Gorman, 2024: Asymmetry of the Distribution of Vertical Velocities of the
737 Extratropical Atmosphere in Theory, Models and Reanalysis. *J. Atmos. Sci.*, **in press**.
- 738 Lapeyre, G., and I. M. Held, 2004: The Role of Moisture in the Dynamics and Energetics of Tur-
739 bulent Baroclinic Eddies. *Journal of the Atmospheric Sciences*, **61**, 1693–1710, [https://doi.org/](https://doi.org/10.1175/1520-0469(2004)061(1693:tromit)2.0.co;2)
740 [10.1175/1520-0469\(2004\)061\(1693:tromit\)2.0.co;2](https://doi.org/10.1175/1520-0469(2004)061(1693:tromit)2.0.co;2).
- 741 Montgomery, M. T., and B. F. Farrell, 1991: Moist surface frontogenesis associated with in-
742 terior potential vorticity anomalies in a semigeostrophic model. *J. Atmos. Sci.*, **48**, 343–368,
743 [https://doi.org/10.1175/1520-0469\(1991\)048\(0343:msfawi\)2.0.co;2](https://doi.org/10.1175/1520-0469(1991)048(0343:msfawi)2.0.co;2).
- 744 Montgomery, M. T., and B. F. Farrell, 1992: Polar low dynamics. *J. Atmos. Sci.*, **49**, 2484–2505,
745 [https://doi.org/10.1175/1520-0469\(1992\)049\(2484:PLD\)2.0.CO;2](https://doi.org/10.1175/1520-0469(1992)049(2484:PLD)2.0.CO;2).
- 746 Moore, R. W., and M. T. Montgomery, 2004: Reexamining the dynamics of short-scale, diabatic
747 rossby waves and their role in midlatitude moist cyclogenesis. *J. Atmos. Sci.*, **61**, 754–768,
748 [https://doi.org/10.1175/1520-0469\(2004\)061\(0754:RTDOSD\)2.0.CO;2](https://doi.org/10.1175/1520-0469(2004)061(0754:RTDOSD)2.0.CO;2).
- 749 Moore, R. W., and M. T. Montgomery, 2005: Analysis of an idealized, three-dimensional diabatic
750 Rossby vortex: A coherent structure of the moist baroclinic atmosphere. *J. Atmos. Sci.*, **62**,
751 2703–2725, <https://doi.org/10.1175/JAS3472.1>.
- 752 Moore, R. W., M. T. Montgomery, and H. C. Davies, 2008: The integral role of a diabatic
753 rossby vortex in a heavy snowfall event. *Mon. Wea. Rev.*, **136**, 1878–1897, [https://doi.org/](https://doi.org/10.1175/2007MWR2257.1)
754 [10.1175/2007MWR2257.1](https://doi.org/10.1175/2007MWR2257.1).
- 755 O’Gorman, P. A., T. M. Merlis, and M. S. Singh, 2018: Increase in the skewness of extratropical
756 vertical velocities with climate warming: fully nonlinear simulations versus moist baroclinic
757 instability. *Quart. J. Roy. Meteor. Soc.*, **144**, 208–217, <https://doi.org/10.1002/qj.3195>.

- 758 O’Gorman, P. A., 2011: The effective static stability experienced by eddies in a moist atmosphere.
759 *J. Atmos. Sci.*, **68**, 75–90, <https://doi.org/10.1175/2010JAS3537.1>.
- 760 Phillips, N., 1954: Energy Transformations and Meridional Circulations associated with simple
761 Baroclinic Waves in a two-level, Quasi-geostrophic Model. *Tellus*, **6**, 273–286, <https://doi.org/10.1111/j.2153-3490.1954.tb01123.x>.
- 763 Schubert, W., and B. Alworth, 1987: Evolution of potential vorticity in tropical cyclones. *Quarterly*
764 *Journal of the Royal Meteorological Society*, **113**, 147–162.
- 765 Vallis, G. K., 2017: *Atmospheric and oceanic fluid dynamics: Fundamentals and large-scale cir-*
766 *culation, second edition*. Cambridge University Press, <https://doi.org/10.1017/9781107588417>.
- 767 Wernli, H., S. Dirren, M. A. Liniger, and M. Zillig, 2002: Dynamical aspects of the life cycle of
768 the winter storm ‘Lothar’ (26-26 December 1999). *Quart. J. Roy. Meteor. Soc.*, **128**, 405–429,
769 <https://doi.org/10.1256/003590002321042036>.
- 770 Zurita-Gotor, P., 2005: Updraft/downdraft constraints for moist baroclinic modes and their im-
771 plications for the short-wave cutoff and maximum growth rate. *J. Atmos. Sci.*, **62**, 4450–4458,
772 <https://doi.org/10.1175/JAS3630.1>.